Supplementary information

Revealing Origin of Shock Growth of Ice Crystal near Equilibrium Melting Pressure: A Dimensional Growth Transition on Dynamic Compression

Yong-Jae Kim[1 #], Yun-Hee Lee[1,2#], Sooheyong Lee[1,2], Hiroki Nada[3*], Geun Woo Lee[1,2*]

[1]*Division of Industrial Metrology, Korea Research Institute of Standards and Science (KRISS), 34113, Republic of Korea*
[2]*Department of Nano Science, University of Science and Technology (UST), Daejeon 34113, Republic of Korea*
[3]*National Institute of Advanced Industrial Science and Technology (AIST), Tsukuba 305-8569, Japan*

[#] Y.-J. Kim and Y.-H. Lee contributed equally to this work.
[*]To whom correspondence should be addressed. E-mail: gwlee@kriss.re.kr, hiroki.nada@aist.go.jp

1. Direct measurement of dDAC movement with a Michelson interferometer

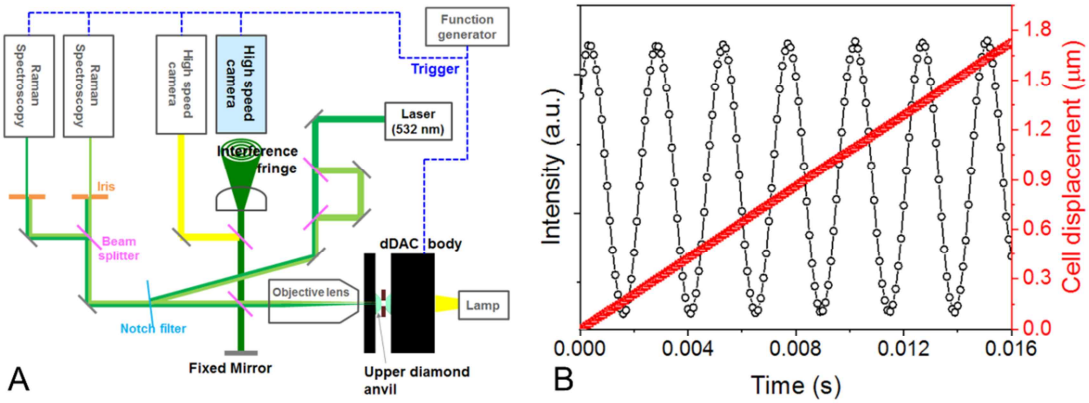

Fig. S1. (*A*) Schematic of dDAC setup with interferometric system. (*B*) Intensity change of interference pattern during compression and resulting cell displacement with time.

Dynamic diamond anvil cell (dDAC) described in previous studies [S1-S3] modulates pressure of sample by piezoelectric actuators; the actuators embedded in the dDAC body cause dynamic (de)compression of a gasket cell, containing sample at a fixed static pressure. We assume that elastic deformation of diamond anvils is negligible and confirm that the lower diamond anvil is strongly fixed on the dDAC body. Thus, the thickness change (Δl) of gasket cell during (de)compression is identical to the moving displacement of the upper diamond anvil. Here, we continuously monitor the movement of the upper anvil with a Michelson interferometer integrated into the dDAC system (see Fig. S1*A*); when piezoelectric

www.pnas.org/cgi/doi/10.1073/pnas.1818122116

actuators push or pull the upper plate of dDAC, on which the upper anvil is mounted, the laser beam reflected from table face of the upper diamond anvil makes dynamic interference pattern with the reference laser beam reflected from the fixed mirror. Power of the incident laser beam was limited to less than 2 mW in order to minimize heating the sample chamber. Intensity variation of the interference pattern recorded with a high-speed camera was fitted with a sinusoidal function to obtain the phase angles (θ) of each data points (Fig. S1*B*). Finally, the displacement (Δl) was calculated as shown in Fig. S1*B* based on the relation of $n\lambda = 2\Delta l$, where λ is the wavelength of incident laser (532 nm) and n is the number of fringe order ($\theta/2\pi$). Even in the hold step formed by applying a constant voltage to the actuators, a minute variation of the interference intensity was recorded and this is converted to standard deviation of the displacement measurement of ±43.92 nm.

2. Quantitative analyses on compression strain and strain rate

Upon compression, sample strain is calculated by dividing the measured displacement (Δl) by the initial gasket thickness (l_0) and subsequently the strain rate is calculated by dividing the strain ($\Delta l/l_0$) with the compression time (t). Assuming that the area of gasket hole (A_0) does not change upon dynamic (de)compression, the measured strain can be same with the volume strain of sample (ε_V), as follows; $\varepsilon_V = \Delta V/V_0 = (\Delta l \cdot A_0)/(l_0 \cdot A_0) = \Delta l/l_0$, where ΔV is the change of the sample volume by dynamic (de)compression, V_0 is initial volume of sample (or gasket cell) at ambient pressure.

In order to measure standard deviations of the strain and the strain rate, we check the measurement uncertainty of the initial gasket thickness and the displacement; the initial gasket thickness measurement carries a uncertainty of ±500 nm and the displacement measurement using the Michelson interferometer carries a uncertainty of ±43.92 nm. Since we generate the trapezoidal function with different compression rates by controlling the cycle period for a given voltage amplitude, standard deviation of the measured strain for each sample chamber has a constant value; the measured strain is $0.0273 \pm 8.70 \times 10^{-4}$ when the anvil displacement of 1.33 μm is considered for the initial cell thickness of 49 μm. The specific chamber dimension and testing condition is same with that for Figs. 1*A* and 1*B*. Here, the standard deviation of the strain rate changes with the compression time; for the strain rate of 0.181, we expect a standard deviation of $\pm 6.00 \times 10^{-3}$ /s.

When the displacement of 1.33 μm corresponding to the driving voltage amplitude of 500 mV (to the piezoelectric actuators) is considered for the compression time in the range of 20 ms ~ 100 s, the compression speed varies from 1.33×10^{-8} to 6.65×10^{-5} m/s. The diffusion speed of water molecules at the equilibrium melting pressure is determined as 5.78 m/s when the diffusivity and interatomic distance between oxygen atoms are given by 1.67×10^{-9} m^2/s and 2.89×10^{-10} m, respectively [S4, S5]. The diffusion speed of water molecules is about 10^4 times faster than the compression speed. Therefore, we can neglect the possibility of inhomogeneous local density variation in the water due to the dynamic compression. In addition, the strain rate by ramping in this study is still much smaller than shock (dynamic) compression ($\gg 10^4$ /s) [S6]. Thus, we believe that this experimental condition is nearly matches hydrostatic condition even though crystal growth occurs inside of the water sample.

3. Ice VI crystal growth in 3-d and 2-d modes under different compression rates

Fig. S2 shows crystal growths for three different compression times (10 s, 250 ms, and 20 ms). Early stages of the crystal growth exhibits same behavior for all the three cases; the rounded 3-d crystal becomes faceted crystal. Here, we can clearly observe that the parallel growth of the {112} plane is faster than the vertical growth; the edges in the culet-parallel direction already forms sharply, while the edges in the vertical direction is still growing (See Fig. S2*A*). The different growth speed of crystal planes is well known phenomenon in early stage of crystal growth due to anisotropic property, which is not an equilibrium shape [S7]. We can observe same phenomenon with 250-ms ramping time which is relatively slow compression (See Fig. S2*B*), and 20-ms ramping time with shock growth (Fig. S2*C*). In the case of 20-ms compression time, once the shock growth occurs from the parallel {112} planes, the overpressure decreases. And thus, there is no longer sufficient driving force available to form the 2-d shock growth in the vertical {112} planes. Therefore, the 2-d shock crystal growth is dominated by the interface property from the crystallographic viewpoint because it occurs after a noticeable faceting of the rounded initial crystal. Also its occurrence can be affected by the sequence of facet plane formation with acute corners and clean edges.

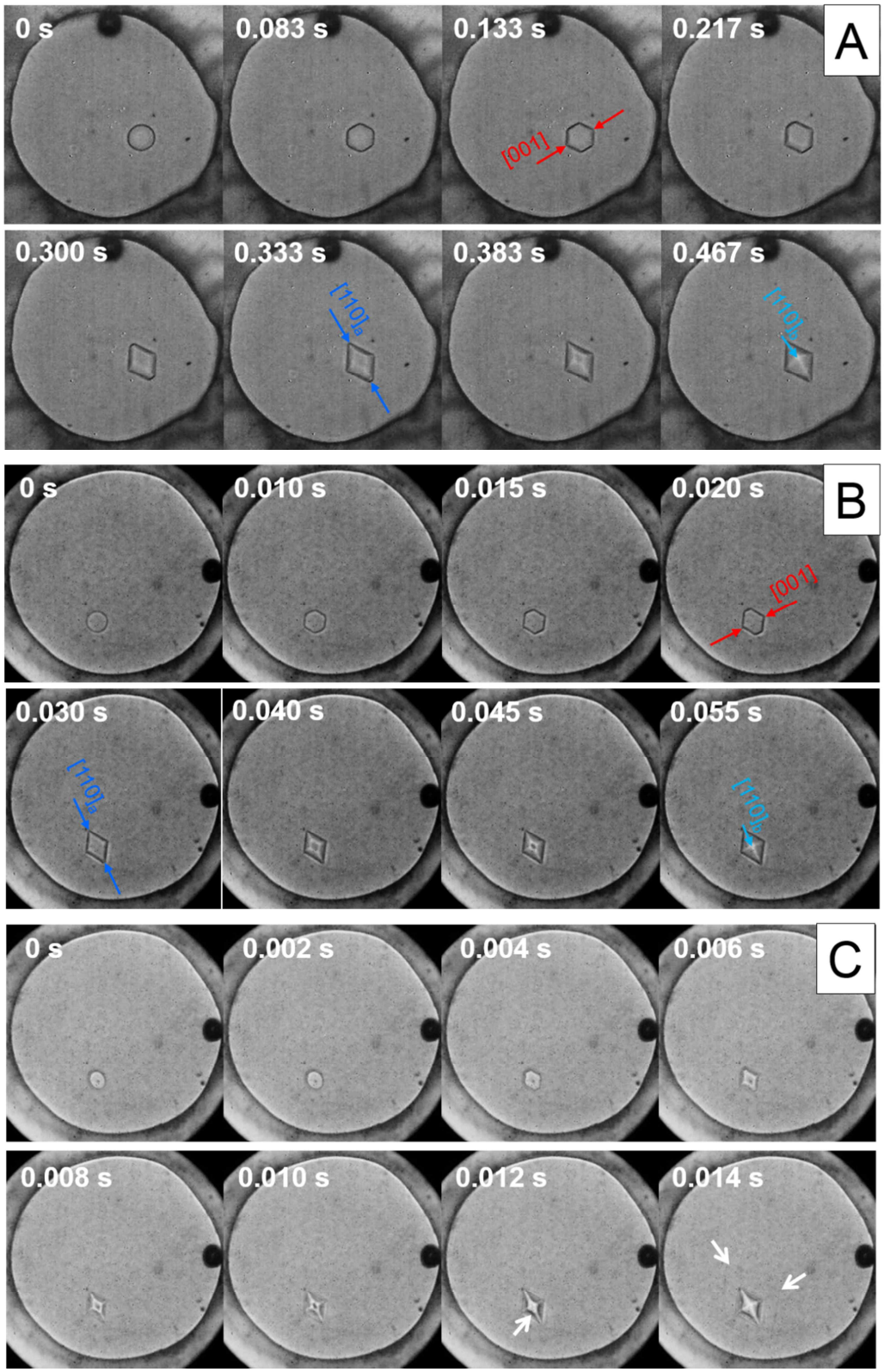

Fig. S2. Regardless of the shock crystal growth, faceting of a rounded starting crystal occurs at the early stage of the compression. A polygonal crystal was shaped from the rounded seed, then grew along the perpendicular direction and finally formed a 3-d faceted polyhedron for (*A*) slow ramping with compressing time of 10 s and (*B*) moderate ramping with compression time of 0.25 s. (*C*) For the case of fast ramping with compression time

of 20 ms, similar faceting process was observed but 2-d shock crystal growth along the in-plane direction occurred before formation of an acute corner along the perpendicular direction.

4. Surface indexing for 3-d faceted and 2-d shock-grown ice VI crystals

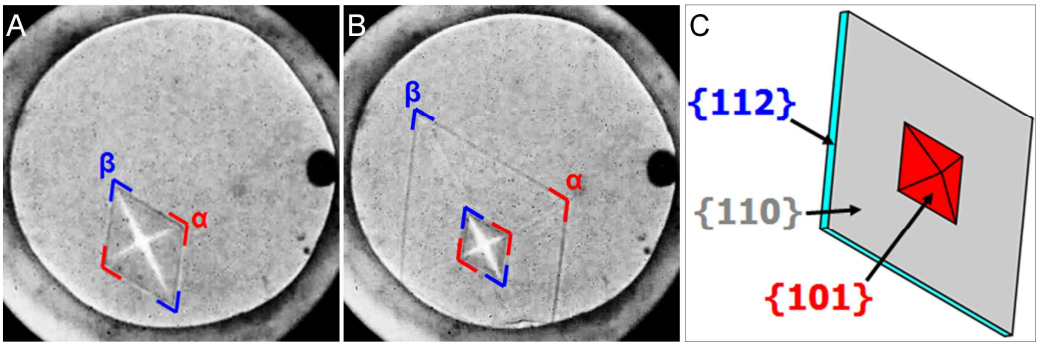

Fig. S3. Morphologies of (*A*) 3-d octahedral and (*B*) 2-d shock-grown rhombic crystals. Both crystals have same corner angles of α = ~114° and β = ~66°. (*C*) Plane indexing for a shock-grown 2-d crystal having 3-d faceted mother crystal at its center.

Crystal planes can be indexed based on geometric characteristics (e.g., corner angles) and crystallographic information. 3-d and 2-d crystals have same corner angles of α= ~114° and β= ~66° (Figs. S3*A* and *B*), indicating an identical crystalline orientation regardless of the growth behavior. For a tetragonal lattice, the included angle (ϕ) between two planes of ($h_1k_1l_1$) and ($h_2k_2l_2$) is given. As a result of various (*hkl*) combination with the lattice parameter of ice VI, a = 0.61812 nm and c = 0.5689 nm [S8], four edge planes forming α and β angles are found to be {112} planes family; the (112) plane have interplanar angle of 113.89° with the $(11\bar{2})$ plane and 66.11° with the $(\bar{1}\bar{1}2)$ plane, which are nearly identical with the experimental α and β angles. While corner direction along the short axis of the octahedral crystal is determined as <001>, those along the long axes are <110>. Finally, morphology of 3-d and 2-d crystal can be described as octahedron covered by {101} crystal planes and rhombic plate covered by four {112} and two {110} crystal planes, respectively. Our indexing for the 3-d crystal is supported by Yamamoto [S9], who also observed {101} ice VI crystal formation under static high-pressure with X-ray precession photographs.

5. Effect of different DAC boundaries (or different chamber thickness) on 2-d shock crystal growth

In order to check the dependence of the 2-d shock crystal growth on boundary condition (or dimensional shape) of the sample chamber, we prepared three gaskets with different initial thicknesses of 17, 53 and 91 μm, but with the same diameter of the gasket hole of 100 μm.

When fast compression of 6.65x10^{-5} m/s (or compression time of 20 ms) is applied, the shock crystal growth is observed for all experimental conditions. Fig. S4 shows the shock crystal grown in the sample chamber with 91 μm in thickness and 100 μm in diameter. This result vindicates that the boundary condition of the sample chamber is not a crucial factor for the shock crystal growth.

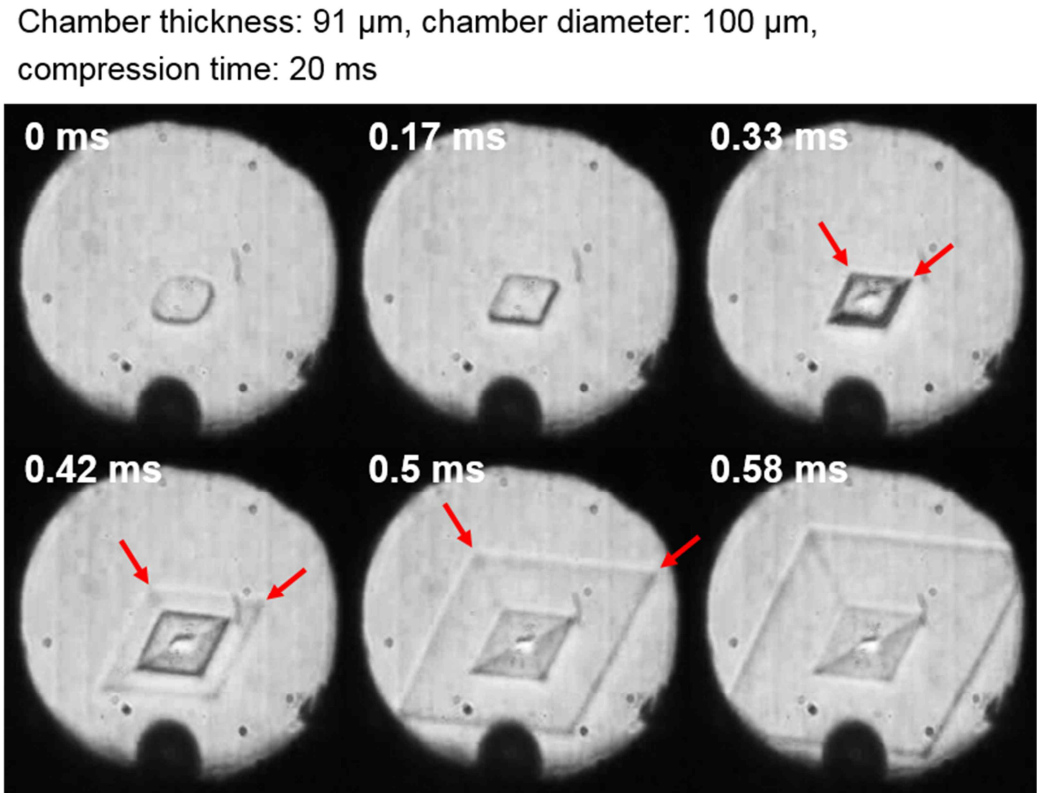

Fig. S4. Faceting and shock crystal growth evolved in a chamber with comparable dimensions along diameter and thickness directions.

6. Estimation of thickness of the 2-d shock grown crystal

If we assume that volumetric growth rates of 3-d and 2-d crystals are identical for short duration, thickness of the 2-d shock grown crystal can be estimated by equating the volume increase of the 3-d crystal with that of the 2-d crystal for a given strain increment. In the case of a rhombohedral plate of the 2-d crystal (Fig. S3*B*), its crystal volume ($V_{2-\mathrm{d}}$) is $2d_{110}\,d_{001}\,h$, where h is the thickness of the 2-d crystal; $V_{2-\mathrm{d}}$ can be simplified into $3.06842 \cdot h \cdot d_{001}^2$. Fig. S5 shows growth displacements in <001> direction, (d_{001}) for 3-d and 2-d growth. Immediately following the shock initiation indicated by an arrow in Fig. S5, the thickness of the 2-d crystal can be calculated by assuming that $\Delta V_{3\text{-d}}$ is equal to $\Delta V_{2\text{-d}}$ for a

short duration.

2-d grown area was analyzed from one or two image frames after the shock moment corresponding to the elapsed time of 0.67 ms for a few crystals. A volume increase of the 3-d facet crystal was also measured from the crystal size change with the same time. Since the 3-d crystal have an octahedral geometry with short <001> and long <110> corners (Fig. S3*A*), its volume ($V_{3-\mathrm{d}}$) can be given by $\frac{4}{3} d_{110}^2 \, d_{001}$, where d_{hkl} is dimension of growing axis along <hkl> directions; $V_{3-\mathrm{d}}$ can be reduced to $3.1381 \cdot d_{001}^3$, considering the lattice parameters of ice VI (a = 0.61812 nm and c = 0.5689 nm [S8]) and the geometric relation of $d_{110} = \frac{\sqrt{2}a}{\mathrm{c}} d_{001}$ in tetragonal lattice. As a result, h is determined to be 132.62±32.07 nm.

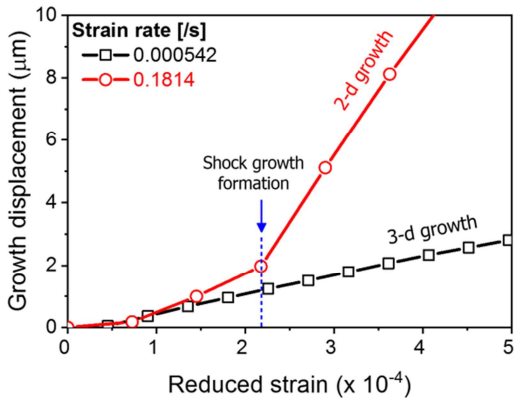

Fig. S5. Growth displacement along <001> corner direction for 3-d and 2-d growth under compression strain rate of 0.000542 /s and 0.1814 /s, respectively. The onset of shock growth is marked by an arrow.

In order to check the latent heat formation by the 2-d shock crystal growth, we consider a simple model system. If a lozenge-shaped, 2-d crystal advances by 5 μm from a 3-d octahedral crystal with a long diagonal axis of 10 μm, the shock-grown volume of the 2-d ice crystal is 12.47 μm^3 (or 9.22x10^{-13} mol) with the nominal thickness of 130 nm. This growth releases the latent heat of 5.37x10^{-9} J. The molar volume and latent heat of ice VI are given as 1.35x10^{-5} m^3/mol and 5.83 kJ/mol, respectively [S10]. If the sample chamber with 100 μm in diameter and 50 μm in thickness is filled with liquid water at 0.96 GPa and ambient temperature, the released latent heat can heat up the water mass of 4.84x10^{-7} g to about 0.0030 K. The molar volume, molar mass and heat capacity of the water are 1.46x10^{-5} m^3/mol, 18.02 g/mol and 3.76 J/(g·K), respectively [S11]. We currently do not have capability to measure such a minor increase in temperature.

7. Uncertainty of pressure measurement

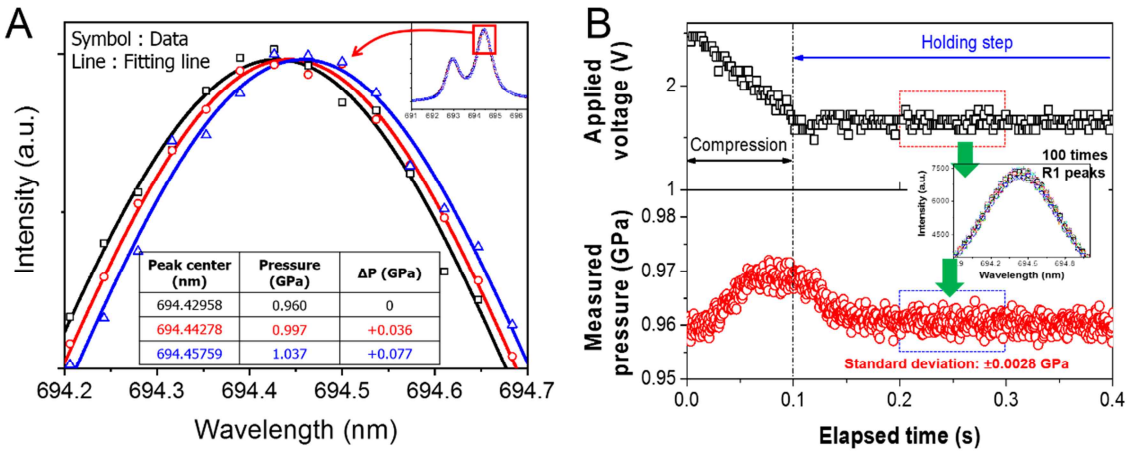

Fig. S6. (*A*) Ruby fluorescence peak (R1) enlarged from peaks in the inset. Red and blue data exhibit peak shift about 0.0132 and 0.0280 nm from equilibrium melting state (black data), corresponding to the overpressure about 0.036 and 0.077 GPa, respectively. (*B*) Standard deviation of the pressure measurement is given by ±2.8 MPa.

Uncertainty of pressure measurement is essentially determined by the resolution of ruby fluorescence peak (R1) measurement. Fig. S6*A* shows the ruby florescence signal during compression, which shows a clear shift of the R1 peak. Our Raman spectroscopy setup provides a pixel resolution of ~0.0368 nm/pixel corresponding to the pressure level of ~0.1 GPa/pixel based on the well-known relation between R1 peak shift and pressure [S12]. However, more precise pressure estimation can be achieved by determining the wavelength centroid of the R1 peak via Gaussian fitting (see Fig. S6*A*). The standard deviation of the pressure is measured at a constant pressure value in the trapezoidal holding regime. More than hundred R1 peaks from the hold regime are analyzed; the standard deviation for the R1 peak center is ±0.0010 nm which corresponds to the pressure standard deviation of ±0.0028 GPa (see Fig. S6*B*). This precise pressure measurement is possible because small ruby balls with micron size are used and fully enclosed by the water at the melting pressure. In addition, the pressure range during the measurement is relatively narrow less than 0.06 GPa during crystal growth, shape distortion (or merging) of the ruby double peaks is negligible; $\Delta\lambda$ between two ruby peaks was 1.4497±0.0015 nm regardless of compression rate or compression cycle.

8. Detection of the onset of the anomalous 2-d shock growth

We detect the onset of the 2-d shock growth by monitoring the sudden increase of growth displacement (see Fig. S7). Interestingly, in spite of the coexistence of water and ice, pressure increases above the equilibrium melting pressure under fast compression (see Fig. S7). Such overpressure implies that crystal growth is delayed even under the significant accumulation of driving force for crystal growth due to a kinetic barrier at the crystal-liquid interface. After the instant of the 2-d shock growth (marked by an arrow in Fig. S7), the overpressure still increases but at a reduced rate. This observation indicates that the anomalous shock growth occurs under local non-equilibrium growth condition.

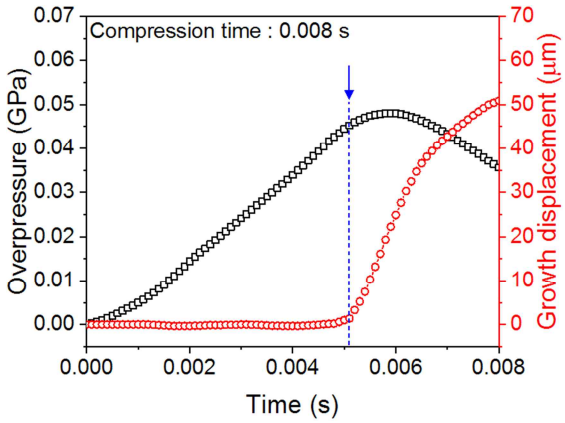

Fig. S7. Simultaneous measurements of both pressure and crystal growth displacement with time. The onset of the 2-d shock growth is marked by an arrow and dashed line.

9. Prediction of effective overpressure and determination of density partitioning at crystal-liquid interface

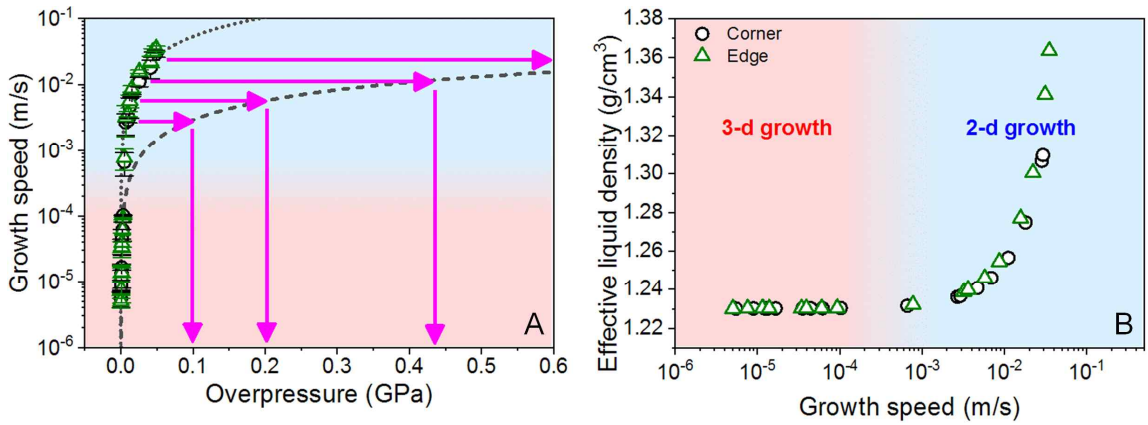

Fig. S8. (*A*) Growth speed vs overpressure plot in Fig. 3*B* with extended overpressure range. The arrows indicate the way to estimate the effective overpressure; (*B*) Plot of effective liquid density with growth speed.

As analogous to the diffusionless solidification in alloy systems via solute trapping [S13-S15], rapid crystal growth of pure substance or colloidal systems under large driving force may accompany defect (or density) trapping [S16, S17]. As a result of the rapidly advancing interface, defects or free volume in liquid can be frozen into solid without defect partitioning at the interface. Thus the partition coefficient (i.e., the ratio of liquid to solid density at interface) becomes close to unity with increasing growth speed. Besides the Aziz's model [S13] on the solute trapping, Jackson et al. developed a power law function for the partition coefficient [S14] and Sobolev extended the solute trapping theories to local non-equilibrium diffusion model [S15]. The partition coefficient under local equilibrium changes into that under local non-equilibrium by considering relaxation effect of solute.

To estimate partition coefficient under fast compression, we attempted to obtain the effective overpressure and the effective water density at the 3-d crystal surface. The effective overpressure necessary for inducing fast growth of the 3-d crystal, which is equivalent to the 2-d shock growth speed, can be estimated from the extrapolation of the growth speed fitting for the 3-d facet crystal (Fig. S8*A*). The predicted value for the effective overpressure is converted to molar volume based on the third-order Birch-Murnaghan equation of state (EOS) with V_0 = 18.145 cm^3/mol, K_0 = 1.986 GPa, and K_0' = 8.66 GPa for water [S18] and supercompressed water (Fig. S8*B*). EOS parameters for ice VI are V_0 = 14.17 cm^3/mol, K_0 = 14.01 GPa, and K_0' = 4 GPa [S19]. Density of water is obtained by dividing the molar volume by the molar mass of water (18.015 g/mol). Finally, partition coefficient is calculated as shown in Fig. 5 which is fitted with the Aziz's model of $k = (k_{Eq} + v/v_{Di})/(1 + v/v_{Di})$ [S13], where k_{Eq} is the equilibrium partition coefficient at melting pressure (0.9106), v is the measured growth speed, v_{Di} is the fitted characteristic speed for density trapping and given by 0.04224 m/s. We note that ice density is assumed to be negligibly affected by the effective overpressure that exists locally within interface regime and thus remains constant (1.35 g/cm^3) during dynamic compressions.

9. Information on MD simulation; potential model and growth speed calculation

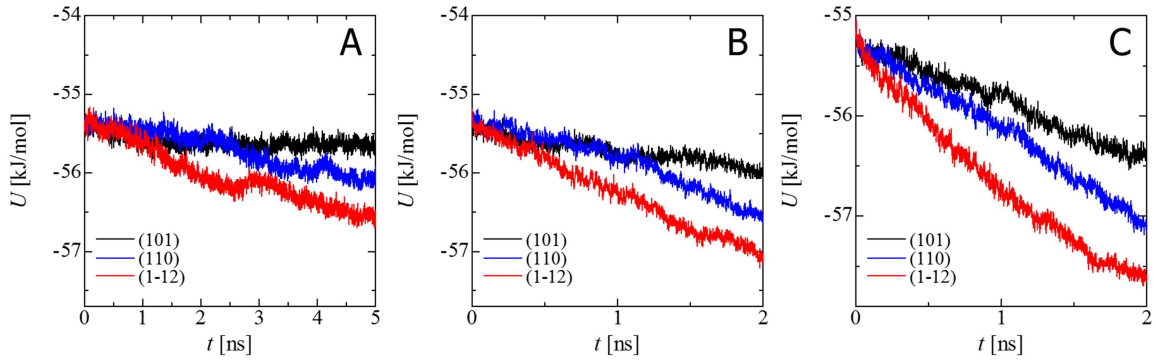

Fig. S9. Time-sequence of the potential energy of the system during growth of (101), (110), and (112) planes under overpressure (ΔP) of 0.08, 0.38, and 0.58 GPa (*A*-*C*).

Growth behavior of (101), (110), and (112) planes of ice VI crystal were explored in MD simulation with the TIP4P/ice potential model [S20]. This potential is available to the temperature-pressure range where ice VI exists. Three simulation systems were prepared for depicting the (101), (110) and (112) planes of an ice VI crystal exposed to supercompressed water. Each system, which consisted of bulk ice and water layers confined in a rectangular-parallelepiped with three-dimensional periodic boundary conditions, was created in the same manner as described in the reference [S21]. Because of the periodic boundary conditions, two ice-water interfaces were created in each system. For both (101) and (110) systems, bulk ice and water layers consist of 2560 and 5120 H_2O molecules, respectively. For the (112) system, bulk ice and water layers consist of 2264 and 4528 H_2O molecules, respectively.

According to the literature [S20], the pressure at which ice VI is in equilibrium with water at 298 K in the TIP4P/Ice model is approximately 1.4 GPa. In our simulation of the (101) system at 298 K, growth occurred at 1.45 GPa and melting occurred at 1.4 GPa, whereas neither growth nor melting occurred at 1.42 GPa. Thus, we assume that the equilibrium pressure is 1.42 GPa. The initial dimensions of each system corresponds to the equilibrium dimensions at 298 K and the equilibrium melting pressure; 4.91×3.39×10.47 nm^3 for the (101) system, 4.68×3.48×10.73 nm^3 for the (110) system, and 5.25×3.14×9.42 nm^3 for the (112) system. The MD simulation for the growth of ice VI was performed for the pressure values of 1.5, 1.75 and 2.0 GPa, corresponding to the overpressure (ΔP) of 0.08, 0.33 and 0.58 GPa at 298 K. Since the MD simulation was performed under isothermal and isobaric condition, the volume of the system decreased as ice VI grew. The crystal growth speed was obtained along different crystal planes by taking the derivatives of the potential energy change with time (Fig.

S9) and summarized in Fig. 4B. According to the reference [S21], crystal growth speed (v) were determined by $\frac{1}{n_{int}\,\Delta u_{iw}}\left(\frac{dU}{dt}\right)\frac{d_l}{N_l}$. Here, $n_{\mathrm{int}} = 2$ is the number of the interfaces included in the system. Δu_{iw} is the shift of the potential energy U when a water molecule in the water region was incorporated into the ice crystal in the system. The value of Δu_{iw} at each overpressure was estimated using $\Delta u_{\mathrm{iw}} = -3.7728\times10^{-5}\times\Delta P - 5.5221\times10^{-4}$, which was determined by performing molecular dynamics simulations of bulk ice VI and water at high pressures separately. d_{l} is the thickness of a molecular layer of the ice plane, and N_{l} is the number of molecules in the layer. $d_{\mathrm{l}}/N_{\mathrm{l}} = 1.3\times10^{-3}$ nm was used for estimation of v for all (101), (110), and (112) planes. The value of dU/dt was measured within whole t range for ΔP = 0.08 and 0.33 GPa and within 0-1.5 ns for ΔP = 0.58 GPa.

The computation was performed using a leap-frog algorithm with a time step of 1 fs [S22]. During each simulation trial, temperature and pressure were maintained at 298 K and each pressure value by means of a method proposed by Berendsen *et al*. [S23]. The thermal and pressure bath constants were set to 0.1 and 2.0 ps, respectively. The simulations were performed with DL_POLY 2.20 [S24]. The Coulomb interaction was estimated by using the Ewald method with an accuracy of 10^{-6}. The real space cutoff distance was set to 10 Å and the Ewald convergence parameter was 0.3208 Å^{-1}. The Lennard-Jones interaction acting between the oxygen atoms of a pair of water molecules was truncated at an intermolecular distance of 10 Å.

10. Information on MD simulation; molecular density profile of interface

The density profile for each plane was generated in the following manner. The system was divided into layers with the thickness of 0.2 Å along the direction normal to the interface, and the time-averaged number of oxygen atoms included in each layer over a period of 0.5 ns from the beginning of the simulation was calculated. The time-average number of oxygen atoms in each layer was normalized by the number of oxygen atoms that produces the density of 1 g/cm^3. Then, the density profile was calculated as the normalized number of oxygen atoms as a function of the layer position in the direction normal to the interface. It may be noted that the density profile of an ice-water interface obtained in an MD simulation does not significantly depend on the system size [S25].

Currently, it is not possible to obtain the density profiles shown in Figs. 4*C* and 4*D* using the experimental data. However, the density, thermal expansion coefficient, and isothermal compressibility of ice VI based on the TIP4P/Ice model are close to the experimental values [S20, S26], which supports that the TIP4P/Ice model correctly reproduces well the structure of ice VI in real systems. Therefore, we do not expect that the present density profiles significantly differ from those in real systems. To confirm the reliability of the density profiles shown in the manuscript, we also analyzed the density profiles using a modified six-site model of H_2O, which was recently proposed for simulations of ice and water [S28]. The modified six-site model provided almost the same density profiles as in the TIP4P/Ice model (Fig. S10). In previous studies [S22, S28], the interface structure obtained by an MD simulation has been successfully used to explain the growth mechanism of ice in real systems, regardless of the type of simulation system (the system for the growth at ice-water interfaces and the system for the free growth of an ice crystal in water). Thus, we believe that the density profiles obtained in this study are reliable and can be used to support the growth mechanism of ice VI explained in the main manuscript.

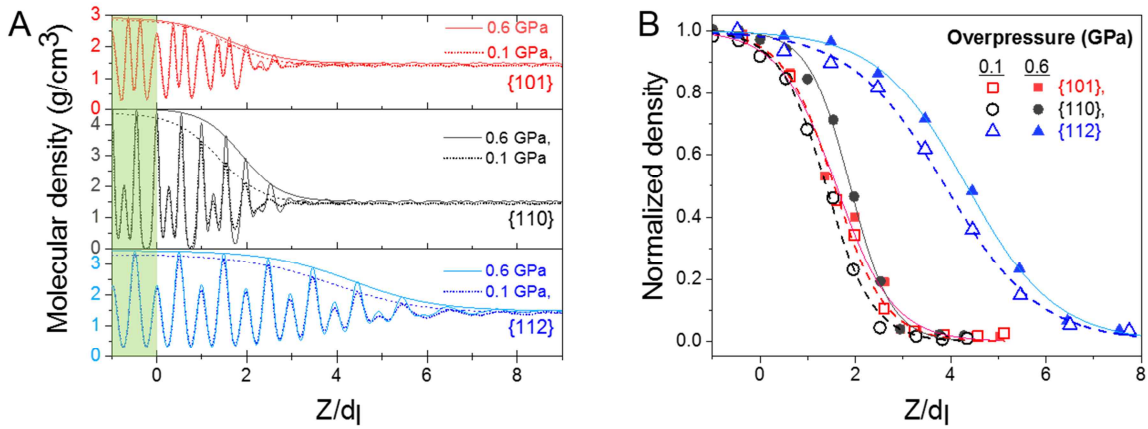

Fig. S10. (*A*) The density profiles at ΔP = 0.1 and 0.6 GPa, which were obtained using the modified six-site model of H_2O [S27]. We assumed that the equilibrium melting pressure of ice VI in the modified six-site model was 1.6 GPa, because ice growth occurred at P > 1.6 GPa and melting occurred at P <1.6 GPa. (*B*) Normalized envelope is fitted with the scaled interface distance, Z relative to the thickness of molecular layer, d_l of each crystal plane.

Notably, the purpose of the present MD simulations was to elucidate the reason for the larger growth speed for the {112} plane as compared to other planes at large ΔP, but not to reproduce the dimensional growth transition from 3-d to 2-d crystal. Since the size and time scales of the MD simulation are much different from those in real systems, it is not possible to numerically reproduce the growth transition from 3-d to 2-d crystal. Strictly speaking, the

growth speed at each plane and crystal morphology would be influenced not only by the growth mechanism at the molecular level but also by macroscopic quantities, such as the latent heat and convection. To discuss the relationship between the molecular-scale growth mechanism and the macroscopic crystal growth in detail, a large-scale macroscopic simulation, such as phase-field simulation [S29] will be required.

In addition, we note that quantum effects in ice and water were not taken into account in the present MD simulation. At present, we do not expect that the simulation results were significantly affected by errors originating from the lack of quantum effects. *Ab initio* water potentials tend to overestimate the melting point of ice [S30, S31]. Confirming the validity of the present simulation results by first-principle MD simulations [S32] or MD simulations with the potential model in which quantum effects are taken into account [S33] will be an important future work.

References

S1. Lee GW, Evans WJ, Yoo C-S (2006) Crystallization of water in a dynamic diamond-anvil cell: Evidence for ice VII-like local order in supercompressed water. *Phys Rev B* 74:134112.

S2. Lee GW, Evans WJ, Yoo CS (2007) Dynamic pressure-induced dendritic and shock crystal growth of ice VI. *Proc Natl Acad Sci USA* 104:9178-9181.

S3. Evans WJ, Yoo CS, Lee GW, Cynn H, Lipp MJ, Visbeck K (2007) Dynamic diamond anvil cell (dDAC): A novel device for studying the dynamic-pressure properties of materials. *Rev Sci Inst* 78:073904.

S4. Mallamace F, Corsaro C, Stanley HE (2012) A singular thermodynamically consistent temperature at the origin of the anomalous behavior of liquid water. *Sci Rep* 2:993.

S5. Katayama Y, Hattori T, Saitoh H, Ikeda T, Aoki K, Fukui H, Funakoshi K (2010) Structure of liquid water under high pressure up to 17 GPa. *Phys Rev B* 81:014109.

S6. Nguyen JH, Orlikowski D, Streitz FH, Holmes NC, Moriarty JA (2004) Specifically prescribed dynamic thermodynamic paths and resolidification experiments. *AIP Conf Proc* 706:1225.

S7. Pieranski P, Sittler L, Sotta P, Imperor-Clerc M (2001) Growth and shapes of a cubic lyotropic liquid crystal. *Eur Phys J E* 5:317-328.

S8. Kuhs WF, Finney JL, Vettier C, Bliss DV (1984) Structure and hydrogen ordering in ices VI, VII and VIII by neutron powder diffraction. *J Chem Phys* 81:3612-3623.

S9. Yamamoto K (1982) A morphological observation of ice VI. *Jpn J Appl Phys* 21:5

S10. Dunaeva AN, Antsyshkin DV, Kuskov OL (2010) Phase diagram of H_2O: Thermodynamic functions of the phase transitions of high-pressure ices. *Sol Syst Res* 44:202.

S11. Abramson et al., (2004) Equation of state of water based on speeds of sound measured in the diamond-

anvil cell. *Geochimica et Cosmochimica Acta* 68:1827-1835.

S12. Mao HK, Xu I, Bell PM (1986) Calibration of the ruby pressure gauge to 800 kbar under quasi-hydrostatic conditions. *J Geophys Res* 91:4673-4676.

S13. Aziz MJ (1982) Model for solute redistribution during rapid solidification. *J Appl Phys* 53:1158-1168.

S14. Jackson KA, Beatty KM, Gudgel KA (2004) An analytical model for non-equilibrium segregation during crystallization. *J Crystal Growth* 271:481-494.

S15. Sobolev SL (2015) Rapid phase transformation under local non-equilibrium diffusion conditions. *Mater Sci Tech* 31:1607-1617.

S16. Tegze G, Tóth GI, Gránásy L (2011) Faceting and branching in 2D crystal growth. *Phys Rev Lett* 106:195502.

S17. Tang S et al. (2014) Phase-field-crystal simulation of nonequilibrium crystal growth. *Phys Rev E* 89:012405.

S18. Lemmon EW, McLinder MO, Friend DG (2016) *Thermophysical properties of fluid systems. NIST Chemistry WebBook: NIST Standard Reference Database*, eds Mallard PJ, W G (NIST, MD), Vol 69.

S19. Bezacier L, Journaux B, Perrillat J-P, Cardon H, Hanfland M, Daniel I (2014) Equations of state of ice VI and ice VII at high pressure and high temperature. *J Chem Phys* 141:104505.

S20. Abascal JLF, Sanz E, Fernádez RG, Bega C (2005) A potential model for the study of ices and amorphous water: TIP4P/Ice. *J Chem Phys* 122:234511.

S21. Allen MP, Tildesley DJ (1987) *Computer Simulation of Liquid* (Clarendon Press, Oxford)

S22. Nada H, Furukawa Y (2005) Anisotropy in growth kinetics at interfaces between proton-disordered hexagonal ice and water: A molecular dynamics study using the six-site model of H_2O. *J Crystal Growth* 283:242-256.

S23. Berendsen HJC, Postma JPM, van Gunsteren WF, DiNola A, Haak JR (1984) Molecular dynamics with coupling to an external bath. *J Chem Phys* 81:3684-3690.

S24. Smith W, Forester TR (1996) DL_POLY 2.0: A General-Purpose Parallel Molecular Dynamics Si mulation Package. *J Mol Graphics* 14:136-141.

S25. Karim OA, Haymet ADJ (1988) The ice/water interface: A molecular dynamics simulation study. *J Chem Phys* 89:6889.

S26. Noya EG, Menduiña C, Aragones JL, Vega C (2007) Equation of state, thermal expansion coefficient, and isothermal compressibility for ices Ih, II, III, V, and VI, as obtained from computer simulation. *J Phys Chem C* 111:15877-15888.

S27. Nada H (2016) Anisotropy in geometrically rough structure of ice prismatic plane interface during growth: Development of a modified six-site model of H_2O and a molecular dynamics simulation. *J Chem Phys* 145:244706.

S28. Nada H (2011) Analysis of ice crystal growth shape under high pressure using molecular dynamics simulation. *Cryst Growth Des* 11:3130-3136.

S29. Kobayashi R (1993) Modeling and numerical simulations of dendritic crystal growth. *Physica D*

63:410-423.

S30. Du S, Yoo S, Li J (2017) Comparison of the melting temperatures of classical and quantum water potential models. *Front Phys* 5:34.

S31. Gillan MJ, Alfè D, Michaelides A (2016) Perspective: How good is DFT for water? *J Chem Phys* 144: 130901.

S32. Schwegler E, Sharma M, Gygi F, Galli G (2008) Melting of ice under pressure. *Proc Natl Acad Sci USA* 105:14779-14783.

S33. Donchev AG, Galkin NG, Illarionov AA, Khoruzhii OV, Olevanov MA, Ozrin VD, Subbotin MV, Tarasov VI (2006) Water properties from first principles: Simulations by a general-purpose quantum mechanical polarizable force field. *Proc Natl Acad Sci USA* 103:8613-8617.